Inorganic Chemistry

pubs.acs.org/IC Article

2D Homologous Series $SrFM_nBiS_{n+2}$ (M = Pb, $Ag_{0.5}Bi_{0.5}$; n = 0, 1) and Commensurately Modulated $Sr_2F_2Bi_{2/3}S_2$

Haijie Chen, Rebecca McClain, Jiahong Shen, Jiangang He, Christos D. Malliakas, Ioannis Spanopoulos, Chi Zhang, Chendong Zhao, Yang Wang, Qiang Li, Duck Young Chung, Xianli Su, Fuqiang Huang, Wai-Kwong Kwok, Christopher Wolverton, and Mercouri G. Kanatzidis*

Cite This: *Inorg. Chem.* 2022, 61, 8233−8240 Read Online

ABSTRACT: We report three new mixed-anion two-dimensional (2D) compounds: $SrFPbBiS_3$, $SrFAg_{0.5}Bi_{1.5}S_3$, and $Sr_2F_2Bi_{2/3}S_2$. Their structures as well as the parent compound $SrFBiS_2$ were refined using single-crystal X-ray diffraction data, with the sequence of $SrFBiS_2$, $SrFPbBiS_3$, and $SrFAg_{0.5}Bi_{1.5}S_3$ defining the new homologous series $SrFM_nBiS_{n+2}$ (M = Pb, $Ag_{0.5}Bi_{0.5}$; n = 0, 1). $Sr_2F_2Bi_{2/3}S_2$ has a different structure, which is modulated with a **q** vector of $1/3b^*$ and was refined in superspace group $X2/m(0\beta0)00$ as well as in the 1 × 3 × 1 superstructure with space group $C2/m$ (with similar results). $Sr_2F_2Bi_{2/3}S_2$ features hexagonal layers of alternating $[Sr_2F_2]^{2+}$ and $[Bi_{2/3}S_2]^{2-}$, and the modulated structure arises from the unique ordering pattern of Sr^{2+} cations. $SrFPbBiS_3$, $SrFAg_{0.5}Bi_{1.5}S_3$, and $Sr_2F_2Bi_{2/3}S_2$ are semiconductors with band gaps of 1.31, 1.21, and 1.85 eV, respectively. The latter compound exhibits room temperature red photoluminescence at ∼700 nm.

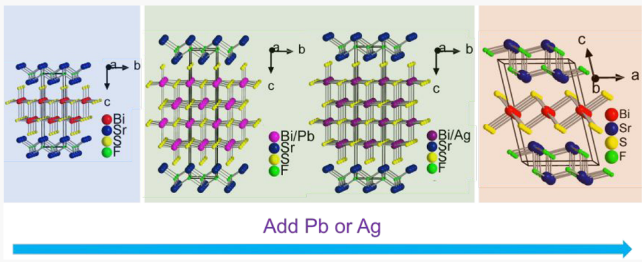

■ INTRODUCTION

Two-dimensional (2D) heteroanionic structures contain different anions that segregate into chemically distinct positively and negatively charged layers. They comprise a large number of phases with properties of broad interest in optoelectronics,[1−3] thermoelectricity,[4,5] superconductivity,[6−8] colossal magnetoresistance,[9] and magnetism.[10−12] The fundamental properties are determined not only by the chemical compositions and bonds within the layers but also by the interactions between the different slabs. Following hard−soft acid−base theory,[13] the distinct layers form as a result of differences in the electronegativity, ionic radius, and polarizability between the cations and anions, where the soft Lewis acid cations are found in the same layer as the soft Lewis base anions and respectively for the hard Lewis acid cations and hard Lewis base anions.[14] Presently, a limited understanding of the synthesis methodologies is required to make specific heteroanionic materials because one has to avoid competing phases, which are homoanionic.

Chalcohalides are a subclass of heteroanioinc materials with unusual structures that result from the bonding preferences of the chalcogenide and halide anions.[15−20] These materials have shown superconductivity, magnetism, light emission, and radiation detection properties.[15−23] There are two types of chalcohalides. The first kind features metal cations with coordination spheres incorporating both the halide and chalcogenide, referred to as heteroleptic coordination. The second kind features different metal cations, each of which has homoleptic coordination environments, with the hard cations binding to hard anions and vice versa, often forming 2D heteroanionic structures. Therefore, combinations of different cations that preferentially bond to certain anions can form a variety of local substructures to form heteroanionic phases. When there is a clear segregation in two chemically different layers forming compounds, they are referred to as heterolayered compounds. Bismuth, for example, is a versatile cation that forms a number of diverse coordination and bonding modes.[24] The most well-known examples are the heterolayered BiQ_2-based series, which can be doped to be superconductors,[25] such as $Bi_4O_4S_3$,[26,27] $LnOBiS_2$ (Ln = rare-earth elements),[28−30] $SrFBiS_2$,[31] $Eu_3Bi_2S_4F_4$,[16] $EuSr_2Bi_2S_4F_4$,[32] and $LaOBiSe_2$.[33] The introduction of Pb and Ag elements into the BiS_2 structure has led to novel mixed-anion compounds, such as $La_2O_2Bi_3AgS_6$[34] and $LaPbBiS_3O$.[35]

In this work, we investigated the heteroanionic phase space with a focus on heterolayered chalcohalides and the tunability of their structures with the introduction of Pb or Ag elements. Three new compounds, $SrFPbBiS_3$, $Sr_{1.58}FAg_{0.21}Bi_{1.21}S_3$, and $Sr_2F_2Bi_{2/3}S_2$, were discovered. We also report a set of synthesis

Received: February 27, 2022
Published: May 17, 2022

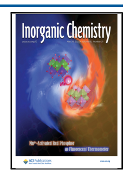

https://doi.org/10.1021/acs.inorgchem.2c00663
Inorg. Chem. 2022, 61, 8233−8240

Table 1. Crystal Data and Structure Refinements for $SrFBiS_2$, $SrFPbBiS_3$, $SrFAg_{0.5}Bi_{1.5}S_3$, and $Sr_2F_2Bi_{2/3}S_2$ at 293 K[a]

empirical formula	$SrFBiS_2$[b]	$SrFPbBiS_3$[c]	$SrFAg_{0.5}Bi_{1.5}S_3$[d]	$Sr_2F_2Bi_{2/3}S_2$[e]
color	black	black	black	red
fw	379.72	619	570.2	416.7
cryst syst	tetragonal			monoclinic
wavelength (Å)	0.71073			
space group, Z	$P4/nmm$, 2			$C2/m$, 6
unit cell dimens				
a (Å)	4.0796(6)	4.1214(6)	4.0899(6)	7.1926(8)
b (Å)	4.0796(6)	4.1214(6)	4.0899(6)	12.4687(10)
c (Å)	13.754(3)	19.716(4)	19.364(4)	10.6446(12)
β (deg)				103.050(8)
volume (Å^3)	228.92(8)	334.90(3)	323.90(11)	929.98(17)
density (calcd) (g/cm^3)	5.509	6.1381	5.8465	4.4648
abs coeff (mm^{-1})	50.774	60.064	51.205	36.634
F(000)	324	520	486	1088
cryst size (mm^3)	0.7631 × 0.2767 × 0.0378	0.6541 × 0.3598 × 0.0141	0.8641 × 0.4236 × 0.0182	0.6348 × 0.3129 × 0.0134
θ range (deg) for data collection	4.445−29.114	4.134−29.091	4.210−29.027	1.96−29.18
index ranges	$-5 \le h \le 5$, $-5 \le k \le 5$, $-18 \le l \le 18$	$-5 \le h \le 5$, $-5 \le k \le 5$, $-25 \le l \le 26$	$-4 \le h \le 5$, $-5 \le k \le 5$, $-26 \le l \le 26$	$-9 \le h \le 9$, $-16 \le k \le 16$, $-14 \le l \le 14$
reflns collected	2163	3175	3082	8963
indep reflns	230 (R_{int} = 0.0607)	332 (R_{int} = 0.0378)	319 (R_{int} = 0.0323)	1308 (R_{int} = 0.082)
completeness (%) to θ = 29.09°	99	99	98	99
refinement method	full-matrix least squares on F^2			
data/restraints/parameters	230/0/15	332/0/21	319/0/22	1308/0/51
goodness-of-fit	3.49	1.60	3.58	3.68
final R indices [$I > 2\sigma(I)$]	R_{obs} = 0.0337, wR_{obs} = 0.0917	R_{obs} = 0.0228, wR_{obs} = 0.0524	R_{obs} = 0.0377, wR_{obs} = 0.1062	R_{obs} = 0.0762, wR_{obs} = 0.1578
R indices (all data)	R_{all} = 0.0408, wR_{all} = 0.0941	R_{all} = 0.0310, wR_{all} = 0.0539	R_{all} = 0.0403, wR_{all} = 0.1063	R_{all} = 0.1037, wR_{all} = 0.1596
ext coeff	1664.31	1698.59	1672.73	5173.35
largest diff peak and hole (e/Å^3)	3.45 and −4.71	2.37 and −2.20	3.91 and −4.31	10.19 and −3.01

[a]$R = \sum||F_o| - |F_c||/\sum|F_o|$; $wR = \{\sum[w(|F_o|^2 - |F_c|^2)^2]/\sum[w(|F_o|^4)]\}^{1/2}$, where $P = (F_o^2 + 2F_c^2)/3$. [b]$w = 1/[\sigma^2(F_o^2) + (0.0149P)^2 + 4.5268P]$. [c]$w = 1/[\sigma^2(F_o^2) + (0.0286P)^2]$. [d]$w = 1/[\sigma^2(F_o^2) + (0.0596P)^2 + 2.2493P]$. [e]$w = 1/[\sigma^2(I) + 0.0004I^2]$.

conditions that give single crystals of $SrFBiS_2$, reported previously only as a polycrystalline powder, which allowed precise structure refinement using single-crystal X-ray diffraction (SXRD).[31] The latter has alternating tetragonal $[SrF]^+$ and $[BiS_2]^-$ slabs and can be considered to be the parent compound of the new homologous phases described here. The introduction of Pb or Ag increases the thickness of the $[BiS_2]^-$ slabs compared to $SrFBiS_2$, forming $[PbBiS_3]^-$ and $[Ag_{0.5}Bi_{1.5}S_3]^-$. Collectively, they define a new homologous family, $SrFM_nBiS_{n+2}$ (M = Pb, $Ag_{0.5}Bi_{0.5}$; n = 0, 1), according to the definition of the homologous series.[36] $Sr_2F_2Bi_{2/3}S_2$, on the other hand, has a different structure and was discovered during the synthetic exploration. This compound features alternating hexagonal $[Sr_2F_2]^{2+}$ and CdI_2-type $[Bi_{2/3}S_2]^{2-}$ layers and surprisingly has a special modulated structure. $SrFPbBiS_3$ and $SrFAg_{0.5}Bi_{1.5}S_3$ were found to be semiconductors with band gaps of 1.31 and 1.21 eV, while $Sr_2F_2Bi_{2/3}S_2$ was also a semiconductor featuring a wider band gap of 1.85 eV with broad defect-based photoluminescence (PL) at ∼700 nm.

■ EXPERIMENTAL SECTION

Reagents. The following chemicals were used as purchased: strontium fluoride (99.995%, Sigma-Aldrich), Pb wire (99.99%, American Elements), Ag particles (99.9%, Sigma-Aldrich), Sr element (99.9%, Sigma-Aldrich), Bi chunks (99.9%, Strem Chemicals), S pellets (99.99%, Sigma-Aldrich), and rubidium chloride (RbCl) powders (99.8%, Sigma-Aldrich).

Synthesis and Crystal Growth. $SrFBiS_2$, $SrFPbBiS_3$, $SrFAg_{0.5}Bi_{1.5}S_3$, and $Sr_2F_2Bi_{2/3}S_2$ were synthesized and grown as single crystals in the RbCl flux. For all compounds, the following combinations of starting materials were loaded into a C-coated fused-silica tube (15 mm o.d. × 13 mm i.d.) and sealed under vacuum (<10^{-3} mbar): for $SrFBiS_2$, SrF_2 (0.188 g, 1.5 mmol), Sr (0.131 g, 1.5 mmol), Bi (0.627 g, 3 mmol), and S (0.192 g, 6 mmol), mixed with RbCl (1 g); for $SrFPbBiS_3$, SrF_2 (0.188 g, 1.5 mmol), Sr (0.131 g, 1.5 mmol), Pb (0.622 g, 3 mmol), Bi (0.627 g, 3 mmol), and S (0.289 g, 9 mmol), mixed with RbCl (1 g); for $SrFAg_{0.5}Bi_{1.5}S_3$, SrF_2 (0.188 g, 1.5 mmol), Sr (0.131 g, 1.5 mmol), Ag (0.162 g, 1.5 mmol), Bi (0.941 g, 4.5 mmol), and S (0.289 g, 9 mmol), mixed with RbCl (1 g); for $Sr_2F_2Bi_{2/3}S_2$, SrF_2 (0.188 g, 1.5 mmol), Sr (0.131 g, 1.5 mmol), Bi (0.209 g, 1 mmol), and S (0.096 g, 3 mmol), mixed with RbCl (1 g). The synthesis and crystal growth were performed by heating the mixture to 1000 °C over 20 h, remaining there for 10 h, and slowly cooling to 700 °C over 60 h, followed by quenching in ice water. The products were obtained in quantitative yields as black plate single crystals for $SrFBiS_2$, $SrFPbBiS_3$, and $SrFAg_{0.5}Bi_{1.5}S_3$ and red plate crystals for $Sr_2F_2Bi_{2/3}S_2$. They were analyzed using scanning electron microscopy−energy-dispersive X-ray spectroscopy (SEM−EDS) and powder X-ray diffraction (PXRD) for phase identification and yield estimation and SXRD for structure analysis.

SXRD. The SXRD data were collected at room temperature (293 K) using a STOE IPDS 2T image-plate diffractometer equipped with graphite-monochromatized Mo Kα radiation (λ = 0.71073 Å). The data were reduced, integrated, and corrected for absorption using the

https://doi.org/10.1021/acs.inorgchem.2c00663
Inorg. Chem. 2022, 61, 8233−8240

STOE *X-AREA* package suite.[37] To solve and refine the crystal structure, the *Jana2006* package was used and the full-matrix least squares on F^2 was employed.[38,39] Analysis of the frames of $Sr_2F_2Bi_{2/3}S_2$ reveals that two sets of spots exist, corresponding to the main diffractions and relatively weak satellites. The structure was refined using a 1 × 3 × 1 superstructure. The summarized crystal data and structure refinements are listed in Tables 1 and S1−S16.

First-Principles Calculations. Vienna ab initio simulation package (*VASP*)[40,41] along with the projector-augmented-wave[42] method was used to perform density functional theory (DFT)[43,44] calculations. The Perdew−Burke−Ernzerhof (PBE)[45,46] generalized gradient approximation was used as the exchange-correlation functional. The plane-wave cutoff energy was set as 520 eV, and the structures were fully relaxed until the total energy converged to within 10^{-6} eV. A Γ-centered k mesh with ≈8000 k points per reciprocal atom (KPPRA) was used to sample the Brillouin zone. The spin−orbit coupling was considered in the performance of DFT calculations. To calculate the band structure of $Sr_2F_2Bi_{2/3}S_2$, a 20-atom primitive cell (Figure S2a) was constructed by simple removal of the Bi atoms in the experimental structure to reach the target composition. To capture the information on the cation-disordered $Sr_2F_2Bi_{2/3}S_2$ structure, a 60-atom special quasi-random structure (SQS) was generated (Figure S2b).[47] We used the Monte Carlo algorithm (mcsqs), implemented in the Alloy Theoretic Automated Toolkit (ATAT), to create the SQS structures.[48] We used a distance-based cutoff of all two-, three-, and four-body clusters with maximum distances of 6, 5, and 4 Å, respectively, to determine the cluster correlations within the SQS. Because the band structures of the SQSs were folded in the Brillouin zone, only the density of states and associated band gaps were calculated for the SQSs.

■ RESULTS AND DISCUSSION

Crystal Structures of $SrFBiS_2$, $SrFPbBiS_3$, and $SrFAg_{0.5}Bi_{1.5}S_3$. The tetragonal $SrFBiS_2$ serves as the parent structure for $SrFPbBiS_3$ and $SrFAg_{0.5}Bi_{1.5}S_3$, whereas the red $Sr_2F_2Bi_{2/3}S_2$ was discovered while investigating the structural tunability of this series. The structure of $SrFBiS_2$ was previously refined using the PXRD data; however, single-crystal growth has not been reported.[31] A representative crystal with the dimensions of ∼100 × 100 × 10 μm^3 is shown in Figure 1a. As listed in Table 1, $SrFBiS_2$, $SrFPbBiS_3$, and $SrFAg_{0.5}Bi_{1.5}S_3$ crystallize in the same space group ($P4/nmm$). Considering the existence of the heavy elements in these materials, the absorption correction effects are probably larger than those used.

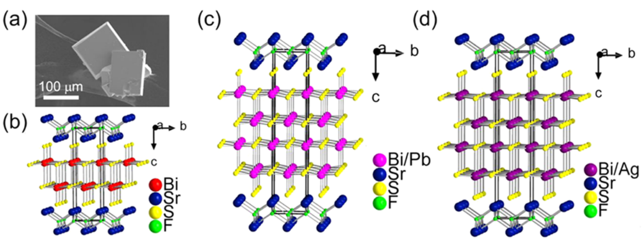

Figure 1. (a) SEM image of an as-synthesized $SrFBiS_2$ single crystal with dimensions of ∼100 × 100 × 10 μm^3. Crystal structures of (b) $SrFBiS_2$, (c) $SrFPbBiS_3$, and (d) $SrFAg_{0.5}Bi_{1.5}S_3$.

The $SrFBiS_2$ structure consists of alternating tetragonal $[BiS_2]^-$ and PbO-type $[SrF]^+$ layers, stacked along the c axis. With the introduction of Pb and Ag in $SrFBiS_2$, the resulting structures of $SrFPbBiS_3$ and $SrFAg_{0.5}Bi_{1.5}S_3$ exhibit mixed occupancies in metal sites and expand along the c axis. After determination of the correct stoichiometry from the crystallographic refinement, the proper ratios of starting materials were used for the synthesis of polycrystalline powders by solid-state reactions in vacuum. Pure phases were successfully obtained, as confirmed by PXRD patterns (Figure S1).

For $SrFPbBiS_3$, the refined occupancies of Bi and Pb were 0.5 and 0.5, within the (Pb/Bi)-S layer. This results in the charge-balanced formula $SrFPbBiS_3$, which is consistent with the composition from SEM−EDS analysis. The Pb and Bi elements appear to be fully statistically disordered, occupying the same crystallographic sites. The summarized crystal data and refinements are listed in Table 1. For $SrFAg_{0.5}Bi_{1.5}S_3$, the occupancies of Bi and Ag were refined as 0.75 and 0.25 within the (Ag/Bi)-S layer, giving the formula $SrFAg_{0.5}Bi_{1.5}S_3$. Differing from the behavior of Pb in $SrFPbBiS_3$, the Ag atom preferentially occupies the interior Bi site (Bi1), as listed in Table S7. The occupancies for Bi1/Ag1 and Bi2/Ag2 are refined as 0.96:0.04 and 0.54:0.46, respectively.

Changes in the cell parameters by the introduction of Pb and Ag are slight in the a and b axes but significant in the c axis, which reflects the expansion of the rock-salt-type Bi/S slabs by one (Pb(Ag)/Bi)S monolayer. Herein, the introduction of Pb in $SrFBiS_2$ enables the stabilization of $SrFPbBiS_3$, which exhibits thicker metal sulfide layers than $SrFBiS_2$, while the positively charged $[SrF]^+$ layer remains intact, playing the same role as that in $SrFBiS_2$.

The formula of $SrFPbBiS_3$ can be written as [SrF][Pb]-$[BiS_{1+2}]$. For $SrFAg_{0.5}Bi_{1.5}S_3$, Ag and Bi are also disordered and contribute jointly to the $[BiS_2]^-$ layers, similar to the role of Ag in Cs−Ag−Bi−Q (Q = S, Se).[49] Considering the rock-salt structure of $AgBiS_2$, the formula of $SrFAg_{0.5}Bi_{1.5}S_3$ can be viewed as $[SrF][Ag_{0.5}Bi_{0.5}][BiS_{1+2}]$.[50] This validates the existence of a new homologous series $SrFM_nBiS_{n+2}$ (M = Pb, $Ag_{0.5}Bi_{0.5}$; n = 0, 1).[36] BiS_2 is the basic building module of the compound, and the layered structures are built up of anionic slabs with increasing thickness.[49,51] The tunability of the structure was subsequently tested through chemical substitutions for Sr as well as increased addition of Pb and Ag. Specifically, Ca and Ba were investigated to substitute Sr in the parent structure as well as in the Pb- or Ag-containing compounds. These attempts were unsuccessful, and they demonstrate that the $[SrF]^+$ layers are crucial to stabilizing $[BiS_2]^-$ layers, most likely because of size considerations ensuring proper lattice matching between the two chemically distinct layers.

Crystal Structure of $Sr_2F_2Bi_{2/3}S_2$. Initially red plate crystals with an elemental ratio of ∼1:1:0.6:1 of Sr, F, Bi, and S were observed as a byproduct in a reaction exploring compounds with higher values of n. The phase was identified as $Sr_2F_2Bi_{2/3}S_2$, and it is not a member of the above-mentioned homologous series because it exhibits a very different formula. Pure $Sr_2F_2Bi_{2/3}S_2$ could be synthesized as a red polycrystalline powder by the solid-state reaction of stoichiometric ratios of starting materials.

For $Sr_2F_2Bi_{2/3}S_2$, SXRD data revealed a commensurately modulated structure along the b axis with a **q** vector of $1/3b^*$. Refinement was well conducted using a 1 × 3 × 1 superstructure (Table 1). It crystallizes into a layered structure with alternating $[Sr_2F_2]^{2+}$ and $[Bi_{2/3}S_2]^{2-}$ layers, as shown in Figure 2. The $[Sr_2F_2]^{2+}$ layer is different from the $[SrF]^+$ layer described above because it displays a hexagonally packed array of atoms (Figure 2c). The $[Bi_{2/3}S_2]^{2-}$ layer shows a hexagonal CdI_2-type architecture (Figure 2d). In the superstructure of $Sr_2F_2Bi_{2/3}S_2$, the Sr−F distances show more different values than the Bi−S distances (Table S12). This suggests that the

https://doi.org/10.1021/acs.inorgchem.2c00663
Inorg. Chem. 2022, 61, 8233−8240

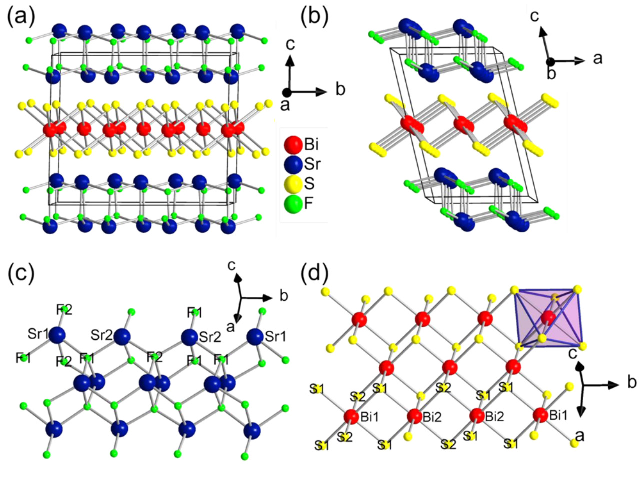

Figure 2. Crystal structure of $Sr_2F_2Bi_{2/3}S_2$ with alternating $[Sr_2F_2]^{2+}$ and $[Bi_{2/3}S_2]^{2-}$ layers along the (a) *a* and (b) *b* axes. (c) ZnS-type $[Sr_2F_2]^{2+}$ layers. (d) CdI_2-type $[Bi_{2/3}S_2]^{2-}$ layers.

modulation is mainly associated with the $[Sr_2F_2]^{2+}$ layers rather than the $[Bi_{2/3}S_2]^{2-}$ layers and presumably originates from a lattice size mismatch between the two different layers. The structure was also refined using the (3 + 1)-dimensional superspace group $X2/m(0\beta0)00$. The results are listed in Tables S13−S16, which are consistent with the above refinement.

Optical Band Gaps, Charge Transport, and Photoluminescence (PL). The optical absorption spectra of the as-synthesized samples are shown in Figure 3. For $SrFBiS_2$,

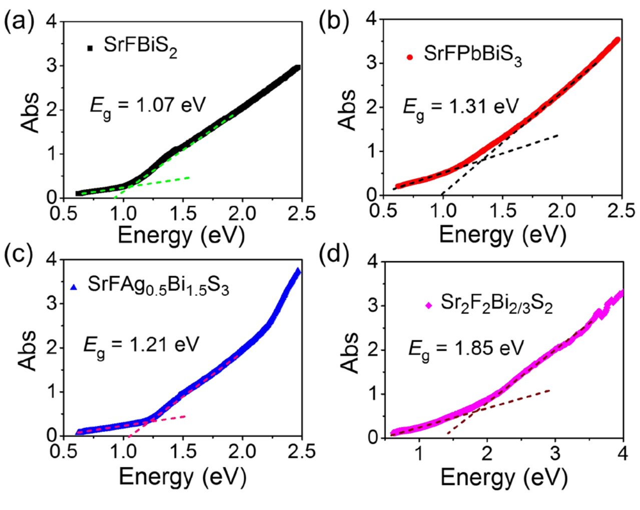

Figure 3. Optical absorption spectra of polycrystalline (a) $SrFBiS_2$, (b) $SrFPbBiS_3$, (c) $SrFAg_{0.5}Bi_{1.5}S_3$, and (d) $Sr_2F_2Bi_{2/3}S_2$.

$SrFPbBiS_3$, and $SrFAg_{0.5}Bi_{1.5}S_3$, the respective band gaps were determined to be 1.07, 1.31, and 1.21 eV. As shown in Figure 3d, $Sr_2F_2Bi_{2/3}S_2$ has a considerably larger band gap of 1.85 eV than the other three compounds, which is consistent with its red color. The shallow optical absorptions evident in the spectra suggest that all samples are indirect-band-gap semiconductors. It is noted that nonlinear behaviors are present in the absorption spectra, which may be a result of the impurities.

Figure 4 shows the charge- and thermal-transport properties of $SrFBiS_2$, $SrFPbBiS_3$, and $SrFAg_{0.5}Bi_{1.5}S_3$. They were obtained from as-synthesized polycrystalline samples con-

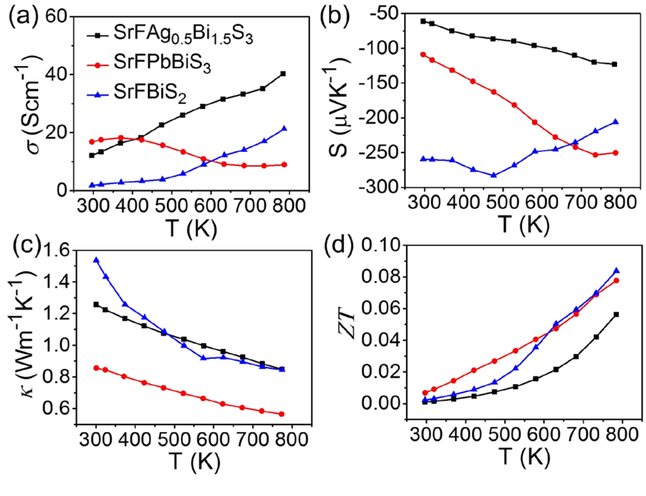

Figure 4. Temperature dependence of the (a) electrical conductivity, (b) Seebeck coefficient, (c) thermal conductivity, and (d) *ZT* values of $SrFBiS_2$, $SrFPbBiS_3$, and $SrFAg_{0.5}Bi_{1.5}S_3$ perpendicular to the pressure direction.

solidated into dense pellets using the spark-plasma-sintering process, and no attempts were made to dope them. The electrical conductivities of $SrFBiS_2$ and $SrFAg_{0.5}Bi_{1.5}S_3$ exhibit typical semiconductor behavior in the temperature range of 300−773 K and increase from 1.79 to 21.2 S/cm and from 12.2 to 40.4 S/cm, respectively (Figure 4a). $SrFPbBiS_3$ shows a different trend, with the electrical conductivity decreasing from 16.8 to 8.9 S/cm with increasing temperature. The Seebeck coefficients of all three samples are negative, suggesting that electrons are the dominant carriers (Figure 4b). Consistent with its higher electrical conductivity, $SrFAg_{0.5}Bi_{1.5}S_3$ has the lowest Seebeck coefficient of −61.1 μV/K at room temperature, compared to those of −108.8 and −259.3 μV/K for $SrFPbBiS_3$ and $SrFBiS_2$.

Figure 4c shows the thermal conductivities of $SrFBiS_2$, $SrFPbBiS_3$, and $SrFAg_{0.5}Bi_{1.5}S_3$. The $SrFPbBiS_3$ and $SrFAg_{0.5}Bi_{1.5}S_3$ samples exhibit lower thermal conductivities between 300 and 773 K, compared to $SrFBiS_2$. The $SrFPbBiS_3$ shows the lowest thermal conductivity of 0.86 W/m·K at 300 K. With increasing temperature, the thermal conductivity decreases to the very low value of 0.56 W/m·K at 773 K. The thermoelectric performances of the three samples are given in Figure 4d. The maximal *ZT* values for $SrFBiS_2$, $SrFPbBiS_3$, and $SrFAg_{0.5}Bi_{1.5}S_3$ were calculated to be 0.08, 0.07, and 0.06 at 773 K, respectively. A greatly improved performance can be anticipated by suitable doping to tune the electrical conductivity, Seebeck coefficient, and thermal conductivity; however, this is beyond the scope of this report.

Single crystals of $Sr_2F_2Bi_{2/3}S_2$ show a weak red room temperature emission centered at ∼700 nm with a full width at half-maximum (fwhm) of ∼200 nm (Figure 5). The PL maximum has a small energy shift of 30 nm from the band gap (Figure 5a) and is believed to originate from a defect center. The defect center provides an energy level close to that of the valence band maximum (VBM) or conduction band minimum (CBM) and contributes to the energy shift. The Bi vacancies in $Sr_2F_2Bi_{2/3}S_2$ may contribute to this and needs more investigation in the future. The PL spectrum looks slightly asymmetric, indicating a potential multiemission feature in this material. To our knowledge, reports of Bi-based chalcogenides with PL emission are scarce and point to the need for detailed

https://doi.org/10.1021/acs.inorgchem.2c00663
Inorg. Chem. 2022, 61, 8233−8240

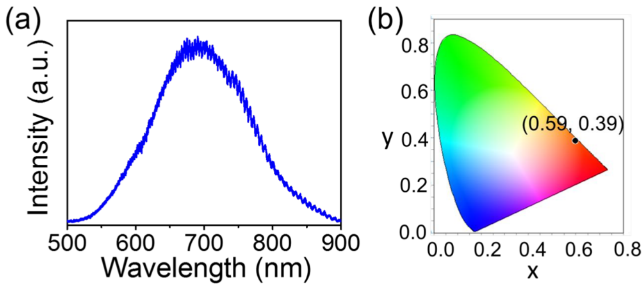

Figure 5. Steady-state PL spectrum of a $Sr_2F_2Bi_{2/3}S_2$ single crystal with an excitation wavelength of 473 nm.

studies about the radiative emission mechanism in this compound.

The corresponding CIE (International Commission on Illumination) chromaticity coordinates are (0.59, 0.49), with a much larger contribution from the red and IR region of the spectrum compared to that from pure white light, which has chromaticity coordinates of (0.33, 0.33). This gives the emission from $Sr_2F_2Bi_{2/3}S_2$ a correlated color temperature (CCT) of 1401 K (warm red light) and a very high color-rendering-index (CRI) value of 88, meaning that this material if optimized could be of interest for indoor lighting applications (Figure 5b). CIE coordinates and CCT values were calculated using the ColorCalculator by OSRAM Sylvania, Inc. CRI quantifies how accurately illuminated colors are reproduced; for indoor lighting, values above 80 are required.

First-Principles Calculations. The electronic band structure and partial density of states (PDOS) of the primitive cell of $Sr_2F_2Bi_{2/3}S_2$ are shown in Figure 6. The results suggest

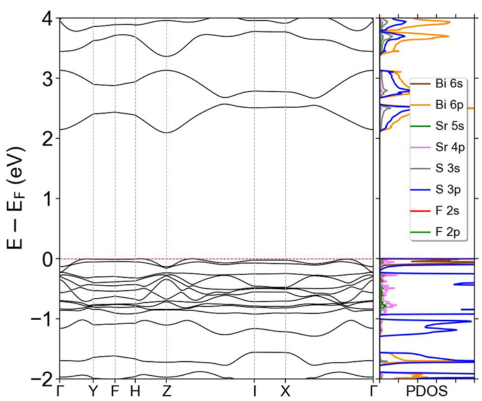

Figure 6. Electronic band structure and PDOS of $Sr_2F_2Bi_{2/3}S_2$.

that the compound is an indirect-band-gap semiconductor with a PBE-calculated band gap of 2.10 eV, and this is consistent with the shallow slope of the optical absorptions revealed by the optical spectra in Figure 3. The CBM is at the Z point of the Brillouin zone. Another band pocket appears at the Γ point near the CBM. The top of the valence band is very flat in energy dispersion, indicating large effective masses and presumably low hole-carrier mobilities. The VBM is located at the middle of the line between Γ and Y, H and Z, Z and I, and X and Γ. It can be seen from the PDOS that the conduction bands and valence bands near the Fermi level are mainly contributed by Bi 6p, S 3p and Bi 6s, S 3p orbitals, respectively. The calculated band gap based on this method of calculation was larger than the measured band gap and is mainly due to the oversimplified primitive structure because we cannot properly simulate the long- and short-range order of partially occupied Bi atoms in the primitive cell. For comparison, a SQS model structure was further calculated to better simulate the cation-disordered $Sr_2F_2Bi_{2/3}S_2$. The densities of states of the SQS $Sr_2F_2Bi_{2/3}S_2$ structure are shown in Figure S3. The calculated band gap of the SQS-modeled structure is still indirect and 0.79 eV, which is smaller than the experimental 1.85 eV value. This is expected and consistent with the fact that the standard PBE functional typically underestimates the electronic band gap of semiconductors.[52]

■ CONCLUSIONS

By introducing Pb or Ag substitutions into the Bi site of the $SrFBiS_2$ structure, we synthesized three new mixed-anion compounds, $SrFPbBiS_3$, $SrFAg_{0.5}Bi_{1.5}S_3$, and $Sr_2F_2Bi_{2/3}S_2$. All are constructed by two building slab fragments of alternating dielectric Sr−F layers and semiconducting M−Bi−S layers. $SrFPbBiS_3$ and $SrFAg_{0.5}Bi_{1.5}S_3$ have tetragonally packed layers and define a new homologous series with the formula of $SrFM_nBiS_{n+2}$ (M = Pb, $Ag_{0.5}Bi_{0.5}$; n = 0, 1). $Sr_2F_2Bi_{2/3}S_2$ has a different structure and exhibits a commensurate superstructure that can be well described with a (3 + 1)-dimensional crystallographic approach. The origin of the superstructure is the Sr^{2+} atoms, which are slightly displaced from their ideal positions imposed by the commensurate wave. $Sr_2F_2Bi_{2/3}S_2$ has a defect-based red PL at room temperature.

■ ASSOCIATED CONTENT

Supporting Information

The Supporting Information is available free of charge at https://pubs.acs.org/doi/10.1021/acs.inorgchem.2c00663.

Experimental details, PXRD patterns of polycrystalline $SrFBiS_2$, $SrFPbBiS_3$, $SrFAg_{0.5}Bi_{1.5}S_3$, and $Sr_2F_2Bi_{2/3}S_2$, computational model of the primitive cell and SQS structures of $Sr_2F_2Bi_{2/3}S_2$, density of states of the SQS $Sr_2F_2Bi_{2/3}S_2$ structure, and structure refinement results (PDF)

Accession Codes

CCDC 2155017−2155019, 2155431, and 2168019 contain the supplementary crystallographic data for this paper. These data can be obtained free of charge via www.ccdc.cam.ac.uk/data_request/cif, or by emailing data_request@ccdc.cam.ac.uk, or by contacting The Cambridge Crystallographic Data Centre, 12 Union Road, Cambridge CB2 1EZ, UK; fax: +44 1223 336033.

■ AUTHOR INFORMATION

Corresponding Author

Mercouri G. Kanatzidis − *Department of Chemistry, Northwestern University, Evanston, Illinois 60208, United States; Department of Materials Science and Engineering, Northwestern University, Evanston, Illinois 60208, United States; Materials Science Division, Argonne National Laboratory, Lemont, Illinois 60439, United States;* orcid.org/0000-0003-2037-4168; Email: m-kanatzidis@northwestern.edu

https://doi.org/10.1021/acs.inorgchem.2c00663
Inorg. Chem. 2022, 61, 8233−8240

Authors

Haijie Chen − *Department of Chemistry, Northwestern University, Evanston, Illinois 60208, United States; Materials Science Division, Argonne National Laboratory, Lemont, Illinois 60439, United States;* orcid.org/0000-0003-3567-1763

Rebecca McClain − *Department of Chemistry, Northwestern University, Evanston, Illinois 60208, United States;* orcid.org/0000-0002-1906-9791

Jiahong Shen − *Department of Materials Science and Engineering, Northwestern University, Evanston, Illinois 60208, United States;* orcid.org/0000-0002-1951-2183

Jiangang He − *Department of Materials Science and Engineering, Northwestern University, Evanston, Illinois 60208, United States;* orcid.org/0000-0001-9643-3617

Christos D. Malliakas − *Department of Chemistry, Northwestern University, Evanston, Illinois 60208, United States;* orcid.org/0000-0003-4416-638X

Ioannis Spanopoulos − *Department of Chemistry, Northwestern University, Evanston, Illinois 60208, United States;* orcid.org/0000-0003-0861-1407

Chi Zhang − *Department of Materials Science and Engineering, Northwestern University, Evanston, Illinois 60208, United States;* orcid.org/0000-0002-6116-5437

Chendong Zhao − *State Key Laboratory of High-Performance Ceramics and Superfine Microstructure, Shanghai Institute of Ceramics, Chinese Academy of Sciences, Shanghai 201800, P. R. China*

Yang Wang − *State Key Laboratory of High-Performance Ceramics and Superfine Microstructure, Shanghai Institute of Ceramics, Chinese Academy of Sciences, Shanghai 201800, P. R. China*

Qiang Li − *State Key Laboratory of Advanced Technology for Materials Synthesis and Processing, Wuhan University of Technology, Wuhan 430070, P. R. China*

Duck Young Chung − *Materials Science Division, Argonne National Laboratory, Lemont, Illinois 60439, United States*

Xianli Su − *Department of Chemistry, Northwestern University, Evanston, Illinois 60208, United States; State Key Laboratory of Advanced Technology for Materials Synthesis and Processing, Wuhan University of Technology, Wuhan 430070, P. R. China;* orcid.org/0000-0003-4428-6461

Fuqiang Huang − *State Key Laboratory of High-Performance Ceramics and Superfine Microstructure, Shanghai Institute of Ceramics, Chinese Academy of Sciences, Shanghai 201800, P. R. China;* orcid.org/0000-0003-0526-5473

Wai-Kwong Kwok − *Materials Science Division, Argonne National Laboratory, Lemont, Illinois 60439, United States*

Christopher Wolverton − *Department of Materials Science and Engineering, Northwestern University, Evanston, Illinois 60208, United States;* orcid.org/0000-0003-2248-474X

Complete contact information is available at: https://pubs.acs.org/10.1021/acs.inorgchem.2c00663

Author Contributions

H.C. and R.M. contributed equally to this work.

Notes

The authors declare no competing financial interest.

■ ACKNOWLEDGMENTS

Research was primarily supported by the U.S. Department of Energy, Office of Science, Basic Energy Sciences, Materials Sciences and Engineering Division (synthesis and structure characterization). R.M. was supported in part by the National Science Foundation (Grant DMR-2003476). SEM−EDS was performed by using of the EPIC, Keck-II, and/or SPID facility(ies) of Northwestern University's NUANCE Center, which has received support from the Soft and Hybrid Nanotechnology Experimental (SHyNE) Resource (NSF Grant ECCS-2025633), the MRSEC program (NSF Grant DMR-1121262) at the Materials Research Center, the International Institute for Nanotechnology (IIN), the Keck Foundation, and the State of Illinois, through the IIN. This work made use of the IMSERC Crystallography facility at Northwestern University, which has received support from the SHyNE Resource (NSF ECCS-2025633), and Northwestern University. The computational resources were provided by the Quest high-performance computing facility at Northwestern University. This work was also supported by the National Natural Science Foundations of China (Grant 22101045).

■ REFERENCES

(1) Hosono, H.; Hirano, M.; Ota, H.; Orita, M.; Hiramatsu, H.; Ueda, K., LnCuO(S,Se,Te) monocrystalline thin film, its manufacturing method, and optical device or electronic device using the monocrystalline thin film. Google Patents, 2008.

(2) Tsai, H.; Nie, W.; Blancon, J.-C.; Stoumpos, C. C.; Asadpour, R.; Harutyunyan, B.; Neukirch, A. J.; Verduzco, R.; Crochet, J. J.; Tretiak, S.; et al. High-efficiency two-dimensional Ruddlesden−Popper perovskite solar cells. *Nature* **2016**, *536* (7616), 312−316.

(3) Soe, C. M. M.; Stoumpos, C. C.; Kepenekian, M.; Traoré, B.; Tsai, H.; Nie, W.; Wang, B.; Katan, C.; Seshadri, R.; Mohite, A. D.; et al. New type of 2D perovskites with alternating cations in the interlayer space,$(C(NH_2)_3)(CH_3NH_3)_nPb_nI_{3n+1}$: Structure, properties, and photovoltaic performance. *J. Am. Chem. Soc.* **2017**, *139* (45), 16297−16309.

(4) Liu, Y.; Zhao, L.-D.; Liu, Y.; Lan, J.; Xu, W.; Li, F.; Zhang, B.-P.; Berardan, D.; Dragoe, N.; Lin, Y.-H.; Nan, C.-W.; Li, J.-F.; Zhu, H. Remarkable Enhancement in Thermoelectric Performance of BiCuSeO by Cu Deficiencies. *J. Am. Chem. Soc.* **2011**, *133* (50), 20112−20115.

(5) Zhao, L.-D.; He, J.; Berardan, D.; Lin, Y.; Li, J.-F.; Nan, C.-W.; Dragoe, N. BiCuSeO oxyselenides: new promising thermoelectric materials. *Energy Environ. Sci.* **2014**, *7* (9), 2900−2924.

(6) Kamihara, Y.; Watanabe, T.; Hirano, M.; Hosono, H. Iron-based layered superconductor $La[O_{1-x}F_x]FeAs$ (x = 0.05−0.12) with $T_{c=}$ 26K. *J. Am. Chem. Soc.* **2008**, *130* (11), 3296−3297.

(7) Chen, X.; Wu, T.; Wu, G.; Liu, R.; Chen, H.; Fang, D. Superconductivity at 43 K in $SmFeAsO_{1-x}F_x$. *Nature* **2008**, *453* (7196), 761−762.

(8) Zhao, J.; Huang, Q.; De La Cruz, C.; Li, S.; Lynn, J.; Chen, Y.; Green, M.; Chen, G.; Li, G.; Li, Z.; et al. Structural and magnetic phase diagram of $CeFeAsO_{1-x}F_x$ and its relation to high-temperature superconductivity. *Nat. Mater.* **2008**, *7* (12), 953−959.

(9) Moritomo, Y.; Asamitsu, A.; Kuwahara, H.; Tokura, Y. Giant magnetoresistance of manganese oxides with a layered perovskite structure. *Nature* **1996**, *380* (6570), 141−144.

(10) McCabe, E. E.; Free, D. G.; Evans, J. S. A new iron oxyselenide $Ce_2O_2FeSe_2$: Synthesis and characterisation. *Chem. Commun.* **2011**, *47* (4), 1261−1263.

(11) Wang, C.-H.; Ainsworth, C. M.; Gui, D.-Y.; McCabe, E. E.; Tucker, M. G.; Evans, I. R.; Evans, J. S. Infinitely Adaptive Transition Metal Oxychalcogenides: The Modulated Structures of $Ce_2O_2MnSe_2$ and $(Ce_{0.78}La_{0.22})_2O_2MnSe_2$. *Chem. Mater.* **2015**, *27* (8), 3121−3134.

(12) Wang, C.-H.; Ainsworth, C.; Champion, S.; Stewart, G.; Worsdale, M.; Lancaster, T.; Blundell, S.; Brand, H. E.; Evans, J. S. Crystal structure and magnetic modulation in β-$Ce_2O_2FeSe_2$. *Physical Review Materials* **2017**, *1* (3), 034403.

(13) Pearson, R. G. Hard and soft acids and bases. *J. Am. Chem. Soc.* **1963**, *85* (22), 3533−3539.

(14) Kageyama, H.; Hayashi, K.; Maeda, K.; Attfield, J. P.; Hiroi, Z.; Rondinelli, J. M.; Poeppelmeier, K. R. Expanding frontiers in materials chemistry and physics with multiple anions. *Nat. Commun.* **2018**, *9* (1), 1−15.

(15) Kabbour, H.; Janod, E.; Corraze, B.; Danot, M.; Lee, C.; Whangbo, M.-H.; Cario, L. Structure and magnetic properties of oxychalcogenides $A_2F_2Fe_2OQ_2$ (A= Sr, Ba; Q= S, Se) with Fe_2O square planar layers representing an antiferromagnetic checkerboard spin lattice. *J. Am. Chem. Soc.* **2008**, *130* (26), 8261−8270.

(16) Zhai, H.-F.; Zhang, P.; Wu, S.-Q.; He, C.-Y.; Tang, Z.-T.; Jiang, H.; Sun, Y.-L.; Bao, J.-K.; Nowik, I.; Felner, I.; et al. Anomalous Eu valence state and superconductivity in undoped $Eu_3Bi_2S_4F_4$. *J. Am. Chem. Soc.* **2014**, *136* (43), 15386−15393.

(17) Islam, S. M.; Malliakas, C. D.; Sarma, D.; Maloney, D. C.; Stoumpos, C. C.; Kontsevoi, O. Y.; Freeman, A. J.; Kanatzidis, M. G. Direct Gap Semiconductors $Pb_2BiS_2I_3$, $Sn_2BiS_2I_3$, and Sn_2BiSI_5. *Chem. Mater.* **2016**, *28* (20), 7332−7343.

(18) He, Y.; Kontsevoi, O. Y.; Stoumpos, C. C.; Trimarchi, G. G.; Islam, S. M.; Liu, Z.; Kostina, S. S.; Das, S.; Kim, J.-I.; Lin, W.; Wessels, B. W.; Kanatzidis, M. G. Defect antiperovskite compounds $Hg_3Q_2I_2$ (Q= S, Se, and Te) for room-temperature hard radiation detection. *J. Am. Chem. Soc.* **2017**, *139* (23), 7939−7951.

(19) Gibson, Q. D.; Dyer, M. S.; Whitehead, G. F.; Alaria, J.; Pitcher, M. J.; Edwards, H. J.; Claridge, J. B.; Zanella, M.; Dawson, K.; Manning, T. D.; Dhanak, V. R.; Rosseinsky, M. J. $Bi_4O_4Cu_{1.7}Se_{2.7}Cl_{0.3}$: Intergrowth of BiOCuSe and Bi_2O_2Se stabilized by the addition of a third anion. *J. Am. Chem. Soc.* **2017**, *139* (44), 15568−15571.

(20) Chen, H.; McClain, R.; He, J.; Zhang, C.; Olding, J. N.; Dos Reis, R.; Bao, J.-K.; Hadar, I.; Spanopoulos, I.; Malliakas, C. D.; et al. Antiferromagnetic Semiconductor BaFMn0. 5Te with Unique Mn Ordering and Red Photoluminescence. *J. Am. Chem. Soc.* **2019**, *141* (43), 17421−17430.

(21) Panella, J. R.; Chamorro, J.; McQueen, T. M. Synthesis and Structure of Three New Oxychalcogenides: $A_2O_2Bi_2Se_3$ (A= Sr, Ba) and $Sr_2O_2Sb_2Se_3$. *Chem. Mater.* **2016**, *28* (3), 890−895.

(22) Huang, H.; Lin, C.; Li, S.; Guo, K.; Zhang, J.; Lyu, W.; Zhang, J.; Xing, J.; Jiang, Y.; Yang, J., Enhancing thermoelectric performance of $SrFBiS_{2-x}Se_x$ via band engineering and structural texturing. *J. Materiomics* **2021**.

(23) Huang, Y.; Dong, Q.; Zhou, M.; Wang, J.; Liao, K.; Zhang, L.; Bai, J.; Cheng, J.; Liu, Q.; Wang, G. Synthesis, structures and physical properties of new transition-metal fluoroselenides $Ba_3F_2MSe_3$ (M = Zn, Cd). *J. Solid State Chem.* **2021**, 122842.

(24) Kanatzidis, M.; Sun, H.; Dehnen, S. *Bismuth—The Magic Element*; American Chemical Society: Washington, DC, 2020.

(25) Mizuguchi, Y. Material Development and Physical Properties of BiS_2-Based Layered Compounds. *J. Phys. Soc. Jpn.* **2019**, *88* (4), 041001.

(26) Mizuguchi, Y.; Fujihisa, H.; Gotoh, Y.; Suzuki, K.; Usui, H.; Kuroki, K.; Demura, S.; Takano, Y.; Izawa, H.; Miura, O. BiS_2-based layered superconductor $Bi_4O_4S_3$. *Phys. Rev. B* **2012**, *86* (22), 220510.

(27) Singh, S. K.; Kumar, A.; Gahtori, B.; Shruti; Sharma, G.; Patnaik, S.; Awana, V. P. Bulk superconductivity in bismuth oxysulfide $Bi_4O_4S_3$. *J. Am. Chem. Soc.* **2012**, *134* (40), 16504−16507.

(28) Mizuguchi, Y.; Demura, S.; Deguchi, K.; Takano, Y.; Fujihisa, H.; Gotoh, Y.; Izawa, H.; Miura, O. Superconductivity in Novel BiS_2-Based Layered Superconductor $LaO_{1-x}F_xBiS_2$. *J. Phys. Soc. Jpn.* **2012**, *81* (11), 114725.

(29) Xing, J.; Li, S.; Ding, X.; Yang, H.; Wen, H.-H. Superconductivity appears in the vicinity of semiconducting-like behavior in $CeO_{1-x}F_xBiS_2$. *Phys. Rev. B* **2012**, *86* (21), 214518.

(30) Demura, S.; Deguchi, K.; Mizuguchi, Y.; Sato, K.; Honjyo, R.; Yamashita, A.; Yamaki, T.; Hara, H.; Watanabe, T.; Denholme, S. J.; et al. Coexistence of Bulk Superconductivity and Magnetism in $CeO_{1-x}F_xBiS_2$. *J. Phys. Soc. Jpn.* **2015**, *84* (2), 024709.

(31) Lei, H.; Wang, K.; Abeykoon, M.; Bozin, E. S.; Petrovic, C. New layered fluorosulfide $SrFBiS_2$. *Inorg. Chem.* **2013**, *52* (18), 10685−10689.

(32) Haque, Z.; Thakur, G. S.; Parthasarathy, R.; Gerke, B.; Block, T.; Heletta, L.; Pottgen, R.; Joshi, A. G.; Selvan, G. K.; Arumugam, S.; Gupta, L. C.; Ganguli, A. K. Unusual Mixed Valence of Eu in Two Materials— EuSr2Bi2S4F4 and Eu2SrBi2S4F4: Mössbauer and X-ray Photoemission Spectroscopy Investigations. *Inorg. Chem.* **2017**, *56* (6), 3182−3189.

(33) Nagao, M.; Tanaka, M.; Watauchi, S.; Tanaka, I.; Takano, Y. Superconducting anisotropies of F-substituted $LaOBiSe_2$ single crystals. *J. Phys. Soc. Jpn.* **2014**, *83* (11), 114709.

(34) Hijikata, Y.; Abe, T.; Moriyoshi, C.; Kuroiwa, Y.; Goto, Y.; Miura, A.; Tadanaga, K.; Wang, Y.; Miura, O.; Mizuguchi, Y. Synthesis, Crystal Structure, and Physical Properties of New Layered Oxychalcogenide $La_2O_2Bi_3AgS_6$. *J. Phys. Soc. Jpn.* **2017**, *86* (12), 124802.

(35) Sun, Y.-L.; Ablimit, A.; Zhai, H.-F.; Bao, J.-K.; Tang, Z.-T.; Wang, X.-B.; Wang, N.-L.; Feng, C.-M.; Cao, G.-H. Design and synthesis of a new layered thermoelectric material LaPbBiS3O. *Inorg. Chem.* **2014**, *53* (20), 11125−11129.

(36) Kanatzidis, M. G. Structural evolution and phase homologies for "design" and prediction of solid-state compounds. *Acc. Chem. Res.* **2005**, *38* (4), 359−368.

(37) *X-AREA, X-SHAPE, and X-RED*; Stoe & Cie GMbH: Darmstadt, Germany, 2009.

(38) Palatinus, L.; Chapuis, G. SUPERFLIP−a computer program for the solution of crystal structures by charge flipping in arbitrary dimensions. *J. Appl. Crystallogr.* **2007**, *40* (4), 786−790.

(39) Petříček, V.; Dušek, M.; Palatinus, L. Crystallographic computing system JANA2006: general features. *Zeitschrift für Kristallographie-Crystalline Materials* **2014**, *229* (5), 345−352.

(40) Kresse, G.; Furthmüller, J. Efficiency of ab-initio total energy calculations for metals and semiconductors using a plane-wave basis set. *Computational materials science* **1996**, *6* (1), 15−50.

(41) Kresse, G.; Furthmüller, J. Efficient iterative schemes for ab initio total-energy calculations using a plane-wave basis set. *Phys. Rev. B* **1996**, *54* (16), 11169.

(42) Blöchl, P. E. Projector augmented-wave method. *Phys. Rev. B* **1994**, *50* (24), 17953.

(43) Hohenberg, P.; Kohn, W. Inhomogeneous electron gas. *Phys. Rev.* **1964**, *136* (3B), B864.

(44) Kohn, W.; Sham, L. J. Self-consistent equations including exchange and correlation effects. *Phys. Rev.* **1965**, *140* (4A), A1133.

(45) Perdew, J. P.; Burke, K.; Ernzerhof, M. Generalized gradient approximation made simple. *Physical review letters* **1996**, *77* (18), 3865.

(46) Kresse, G.; Joubert, D. From ultrasoft pseudopotentials to the projector augmented-wave method. *Physical review b* **1999**, *59* (3), 1758.

(47) Zunger, A.; Wei, S.-H.; Ferreira, L.; Bernard, J. E. Special quasirandom structures. *Phys. Rev. Lett.* **1990**, *65* (3), 353.

(48) Van De Walle, A. Multicomponent multisublattice alloys, nonconfigurational entropy and other additions to the Alloy Theoretic Automated Toolkit. *Calphad* **2009**, *33* (2), 266−278.

(49) Zhao, J.; Islam, S. M.; Hao, S.; Tan, G.; Stoumpos, C. C.; Wolverton, C.; Chen, H.; Luo, Z.; Li, R.; Kanatzidis, M. G. Homologous Series of 2D Chalcogenides Cs−Ag−Bi−Q (Q= S, Se) with Ion-Exchange Properties. *J. Am. Chem. Soc.* **2017**, *139* (36), 12601−12609.

(50) Rathore, E.; Juneja, R.; Culver, S. P.; Minafra, N.; Singh, A. K.; Zeier, W. G.; Biswas, K. Origin of ultralow thermal conductivity in n-type cubic bulk AgBiS2: soft Ag vibrations and local structural distortion induced by the Bi 6s2 lone pair. *Chem. Mater.* **2019**, *31* (6), 2106−2113.

(51) Hsu, K.-F.; Lal, S.; Hogan, T.; Kanatzidis, M. G. $CsPb_3Bi_3Te_8$ and $CsPb_4Bi_3Te_9$: low-dimensional compounds and the homologous series $CsPb_mBi_3Te_{5+m}$. *Chem. Commun.* **2002**, No. 13, 1380−1381.

(52) Zhang, Y.; Yuan, X.; Sun, X.; Shih, B.-C.; Zhang, P.; Zhang, W. Comparative study of structural and electronic properties of Cu-based multinary semiconductors. *Phys. Rev. B* **2011**, *84* (7), 075127.

https://doi.org/10.1021/acs.inorgchem.2c00663
Inorg. Chem. 2022, 61, 8233−8240